communications materials

ARTICLE

https://doi.org/10.1038/s43246-023-00369-0 OPEN

Design of acoustic absorbing metasurfaces using a data-driven approach

Hamza Baali [1✉], Mahmoud Addouche [2✉], Abdesselam Bouzerdoum[1,3✉] & Abdelkrim Khelif [2✉]

The design of acoustic metasurfaces with desirable properties is challenging due to their artificial nature and the large space of physical and geometrical parameters. Until recently, design strategies were primarily based on numerical simulations based on finite-element or finite-difference time-domain methods, which are limited in terms of computational speed or complexity. Here, we present an efficient two-stage data-driven approach for analyzing and designing membrane-type metasurface absorbers with desirable characteristics. In the first stage, a forward model consisting of a neural network is trained to map an input, comprising the membrane parameters, to the observed sound absorption spectrum. In the second stage, the learned forward model is inverted to infer the input parameters that produce the desired absorption response. The metasurface membrane parameters, which serve as input to the neural network, are estimated by minimizing a loss function between the desired absorption profile and the output of the learned forward model. Two devices are then fabricated using the estimated membrane parameters. The measured acoustic absorption responses of the fabricated devices show a very close agreement with the desired responses.

[1] Division of Information and Computing Technology, College of Science and Engineering, Hamad Bin Khalifa University, Doha, Qatar. [2] Institut FEMTO-ST, CNRS, Université de Bourgogne Franche-Comté 15B Avenue des Montboucons, CEDEX, Besançon, France. [3] School of Electrical, Computer and Telecommunications Engineering, University of Wollongong, Wollongong, Australia. ✉email: hbaali@hbku.edu.qa; mahmoud.addouche@femto-st.fr; abouzerdoum@hbku.edu.qa; abdelkrim.khelif@femto-st.fr

The first successful fabrication of metamaterials by Smith et al.[1] two decades ago revolutionized the conventional view of electromagnetic and acoustic wave propagation. It opened the doors to engineer new materials with variable properties not found in natural materials[2–4]. In essence, metamaterials are artificially structured composite materials characterized by built-in locally resonant structures (LRS). These structures restrain/localize strongly oscillating acoustic or electromagnetic fields in the bulk of the structured materials or on the surface, in the case of metasurfaces, to specific frequencies. The presence of these LRSs allows the control and modulation of incident waves at subwavelength frequency.

Over the past two decades, various metamaterials and metasurfaces have been developed with new acoustic properties: acoustic cloaking[5–7], complete sound reflection and transmission[8–10], complete sound absorption[11–17], and wavefront tailoring[18]. This study concerns sound absorption applications in which conventional approaches rely on materials with limited acoustic performance, such as glass, wool, and perforated panels backed by air cavities[19–21]. These conventional absorbers are characterized by thicknesses having wavelengths in the audible range, which require large mass, limiting the scope of their applications and efficiency. One innovative way to overcome this limitation is using decorated metasurface membranes that can achieve nearly total absorption at low frequency with dimensions much smaller than the wavelength of incident sound waves.

Until recently, however, the analysis of metasurface-based absorbers was primarily based on numerical simulations of physics-based models using either Finite Element methods (FEM) via solvers such as the COMSOL Multiphysics or through finite-difference time-domain (FDTD) methods. The former approach can model complex scenarios and geometries at the cost of slow simulation. This limitation adds to the inconvenience of the black-box nature of the calculations of these commercial packages, which can only provide a posteriori explanation. By contrast, the latter approach is appropriate only for scenarios of low to moderate complexity[22]. The fast development of deep learning techniques in the last decade coupled with the increasing computing power and the growth in data availability has made them a feasible surrogate of FEM for the analysis of acoustic wave systems, both in the time and in the frequency domains[23–26]. Deep learning is based on universal function approximators leveraged to specific problems through learning from data. This data is usually generated from high-fidelity numerical simulations or through physical experiments. One significant advantage of these data-driven approaches is that they do not require knowledge of the governing equations of the system and are much faster than physics-based simulations.

The inverse design of metasurfaces is a high-dimensional non-convex optimization problem that seeks to find optimal metamaterial parameters to achieve a desired behavior. Conventional approaches rely either on nonlinear optimization approaches, such as genetic algorithms, or heuristic methods. Nonlinear optimization approaches are computationally expensive due to repeated sampling and are susceptible to convergence failure. On the other hand, heuristic approaches cannot systematically search a large design space as they rely heavily on trial and error and extensive experimentation[27]. The emergence of new data-driven approaches in recent years has led to a shift in the design paradigm of metamaterials[28–30].

The idea of inverse design using data-driven approaches was initially proposed to analyze neural network architectures[31,32]. The adaptive control community used these approaches to circumvent the limitations and unfeasibility of direct inverse modeling of dynamical systems, which is an ill-posed problem in the Hadamard sense[33]. These approaches have recently gained significant attention in electromagnetic and acoustic metamaterials[34–36]. Popular inverse design approaches include iterative gradient-based and indirect inversion using tandem configuration. In this configuration, a particular inverse solution of an already trained network is connected in series with another network to accomplish an auto-association task (learning an identity mapping across the composite network). In this setup, the forward model allocates one output to each frequency sampling point in the absorption spectrum which leads to significant number of free parameters[37,38]. Other alternative inversion approaches include direct inverse design and global optimization algorithms enabled by generative neural network approaches and neural network inversion through constrained optimization formulations[39–41].

This paper deploys a data-driven approach for forward modeling and inverse design of membrane-based metasurface absorbers. By observing the metasurface parameters (input) and the sound absorption spectrum (output), a forward neural network model learns a nonlinear function that maps inputs to outputs through the minimization of the prediction error. Once trained, the neural network model reduces the high computational demands of conventional forward physics simulations into a single forward pass. We demonstrate the effectiveness of the learned model by producing accurate outputs from parameters that were not used in the training phase. The learned model is then inverted to estimate the membrane parameters (input) that yield the desired response. The inversion is cast as an optimization problem by minimizing the error between the desired response and the predicted output. The objective is to find the set of membrane parameters that minimize the prediction error over a set of frequencies while keeping the forward model parameters (weights and biases) fixed. The proposed inversion approach provides flexibility in optimization, enabling consideration of only the desired absorption at a specific frequency or range of frequencies of interest. In contrast, the tandem architecture does not allow for such specificity. Furthermore, since the inverse problem is purely an optimization-based approach, there is more flexibility to vary the objective function or introduce appropriate constraints, e.g., adding a regularization term without having recourse to retraining of the entire model.

Results and discussion

Forward and inverse modeling. In the following, we describe the forward and inverse models adopted in this study. First, a forward model is learned by training a neural network to predict the sound absorption spectrum, using the membrane's physical parameters and the frequency as input. Second, an inverse model is learned indirectly using the forward model to find the membrane parameters which produce a desired sound absorption profile.

The forward model. An L layer feedforward neural network, with N inputs ($\boldsymbol{x}\in\mathbb{R}^N$) and one output ($y\in\mathbb{R}$), is trained to approximate the physical model, $\boldsymbol{\Phi}(\boldsymbol{x})$, that generates the training data. The network realizes a composite function, which can be expressed as:

$$\boldsymbol{f}(\boldsymbol{x};\boldsymbol{\theta}) = \boldsymbol{f}_L(\boldsymbol{f}_{L-1}(\cdots \boldsymbol{f}_i(\cdots \boldsymbol{f}_1(\boldsymbol{x})))), \tag{1}$$

where $\boldsymbol{\theta}$ denotes the network free parameters and $\boldsymbol{f}_i, i = 1, \ldots, L$, is a vector-valued function, $\boldsymbol{f}_i: \mathbb{R}^{N_{i-1}}\mathbb{R}^{N_i}$. The expression (1) means that the output $\boldsymbol{y}_i$ of each function $\boldsymbol{f}_i$ becomes the input to the following function. Each of these functions comprise two parts: a linear affine transformation $(\boldsymbol{W}_i\boldsymbol{y}_{i-1} + \boldsymbol{b}_i)$ and a nonlinear elementwise activation function $h(\cdot)$. The output $\boldsymbol{y}_i$ of $\boldsymbol{f}_i$ can be expressed as follows:

$$\boldsymbol{y}_i = \boldsymbol{f}_i(\boldsymbol{y}_{i-1};\boldsymbol{\theta}_i) = h(\boldsymbol{W}_i\boldsymbol{y}_{i-1}+\boldsymbol{b}_i) =, i = 1, \cdots L, \text{where } \boldsymbol{y}_0 = \boldsymbol{x}. \tag{2}$$

The parameters $\boldsymbol{\theta}_i$ represent the network parameters comprising the weights $(\boldsymbol{W}_i\mathbb{R}^{N_{i-1}\times N_i})$ and biases $(\boldsymbol{b}_i\mathbb{R}^{N_i})$. Popular

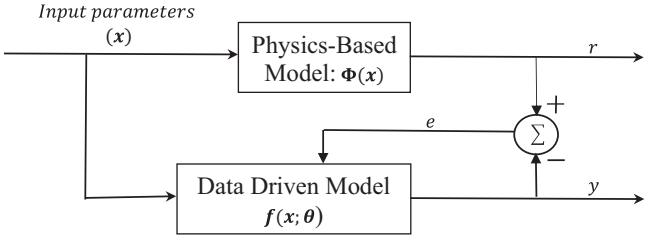

Fig. 1 Block diagram of the forward model learning from the inputs and outputs of the physics-based model. The same input, $\boldsymbol{x}$, is applied to the system, $\boldsymbol{\Phi(x)}$, and the network, $\boldsymbol{f(x;\theta)}$. The desired network weights are found by minimizing a loss function of the prediction error $e = r - y$.

activation functions $h(\cdot)$ include the sigmoid, hyperbolic tangent, and the ReLU functions.

The training involves adjusting the network parameters to minimize a loss function that measures the discrepancy between the network output $y = y_L = \boldsymbol{f(x;\theta)}$ and the desired (ground-truth) output $r = \boldsymbol{\Phi(x)}$ when subjected to the same input, as summarized in Fig. 1.

Given a training dataset D of P typical input and desired output samples $\left\{\boldsymbol{x}^{(i)}, r^{(i)}\right\}_{i=1}^{P}$, where $r^{(i)} = \boldsymbol{\Phi}\left(\boldsymbol{x}^{(i)}\right)$. The network input vector $\boldsymbol{x}^{(i)} = [x_1^{(i)}, x_2^{(i)}, , x_N^{(i)}]^{\boldsymbol{T}}$ comprises the frequency $f^{(i)} = x_1^{(i)}$ and the membrane parameters $\boldsymbol{x}_{2:N}^{(i)} = [x_2^{(i)}, \cdots, x_N^{(i)}]^T$. The task of training a network is to find the best set of parameters (i.e., weights) $\boldsymbol{\theta}^*$ that minimize the mean sum of squares of the network errors over the training set:

$$g(\boldsymbol{\theta}) = \frac{1}{P}\sum_{i=1}^{P}\left(r^{(i)} - y^{(i)}\right)^2 = \frac{1}{P}\sum_{i=1}^{P}\left(r^{(i)} - \boldsymbol{f}(\boldsymbol{x}^{(i)};\boldsymbol{\theta})\right)^2 \tag{3}$$

There exist several optimization techniques to minimize $g(\boldsymbol{\theta})$, such as the Gradient-descent and its variants, Newton's method, and the Levenburg-Marquard algorithm. Most Gradient-descent-like methods involve recursive calculation of the partial derivatives of the loss function g with respect to the network parameters $\boldsymbol{\theta}$ and then use of these derivatives to update the network parameters in the direction that reduces the overall loss g, i.e., the negative gradient direction. The standard gradient-descent update rule for the weights has the form:

$$\boldsymbol{\theta}^{(k+1)} = \boldsymbol{\theta}^{(k)} - \eta\nabla_{\boldsymbol{\theta}} g\left(\boldsymbol{\theta}^{(k)}\right), \tag{4}$$

where $(0<\eta)$ is the learning rate and $\nabla_{\boldsymbol{\theta}}$ is the gradient operator with respect to $\boldsymbol{\theta}$. In practice, the partial derivative forming the gradient $\nabla_{\boldsymbol{\theta}}$ are calculated using the backpropagation algorithm, an efficient algorithm that exploits the composite and the differentiability nature of $\boldsymbol{f}$ to compute the derivatives in reverse mode according to the chain rule.

The inverse model. In this part, we aim to estimate the metamaterial parameters $\boldsymbol{x}_{2:N}$ for which the earlier learned forward model $\boldsymbol{f(x;\theta^*)}$ approximates a 'fictitious' desired sound absorption profile ($\boldsymbol{r}^d = [r_1, r_2, \cdots, r_m, \cdots, r_M]^T$) specified by the user, where r_m is the desired absorption coefficient at frequency f_m. Let $\boldsymbol{y} = [y_1, y_2, \cdots y_M]^T$ be the actual network output sound absorption profile as a function of frequency when its inputs are $\left\{[f_m, \boldsymbol{x}_{2:N}]^T\right\}_{m=1}^{m=M}$. The problem of inverting a neural network model can be then cast as an optimization problem over the network inputs $\boldsymbol{x}_{2:N}$:

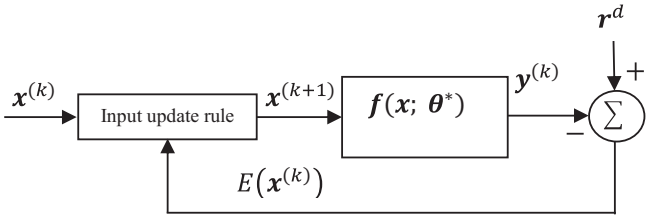

Fig. 2 Iterative inversion of the forward model. The prediction error is backpropagated through the forward model to calculate the gradient with respect to the input parameters. These are iteratively adjusted instead of its weights which are held constants.

$$\min_{\boldsymbol{x}_{2:N}} E(\boldsymbol{x}) = \min_{\boldsymbol{x}_{2:N}} ||\boldsymbol{r}^d - \boldsymbol{y}(\boldsymbol{x})||^2 = \min_{\boldsymbol{x}_{2:N}} \sum_{m=1}^{M} ||r_m - \boldsymbol{f}\left(\left[f_m, \boldsymbol{x}_{2:N}\right]^{\boldsymbol{T}}; \boldsymbol{\theta}^*\right)||^2 \tag{5}$$

An efficient way to solve (5) uses gradient-based optimization whereby the gradient $\nabla_{\boldsymbol{x}}$ with respect to (w.r.t.) the network input elements $x_2, x_2, \ldots, x_N$ are calculated using a variant of the backpropagation algorithm similar to the one used in the training of the forward model. The partial derivative of $E(\boldsymbol{x})$ w.r.t. x_i $(i = 2, \ldots, N)$ is given by

$$\frac{\partial E(\boldsymbol{x})}{\partial x_i} = \frac{\partial||\boldsymbol{r}^d - \boldsymbol{f}(\boldsymbol{x},\boldsymbol{\theta}^*)||^2}{\partial x_i} = 2\left(\boldsymbol{r}^d - \boldsymbol{f}(\boldsymbol{x},\boldsymbol{\theta}^*)\right)\frac{\partial \boldsymbol{f}(\boldsymbol{x},\boldsymbol{\theta}^*)}{\partial x_i}, i = 2, 3, \cdots, N. \tag{6}$$

Since the first elements of $\boldsymbol{x}$ is the frequency f_m, it is not included in the optimization search for the input parameters. The update rule adjusts iteratively the remaining elements $\boldsymbol{x}_{2:N}$ to minimize the difference between the desired outputs r_m and the actual network outputs $y_m = \boldsymbol{f}(\left[f_m, \boldsymbol{x}_{2:N}\right]^{\boldsymbol{T}}, \boldsymbol{\theta}^*)$ such that:

$$\boldsymbol{x}_{2:N}^{(k+1)} = \boldsymbol{x}_{2:N}^{(k)} - \eta\nabla_{\boldsymbol{x}} E\left(\boldsymbol{x}_{2:N}^{(k)}\right) \tag{7}$$

Figure 2 summarizes the computation of the gradient $\nabla_{\boldsymbol{x}}$ using a variant of the backpropagation algorithm, where the network inputs are adjusted instead of its parameters which are held constant.

The iterative network inversion algorithm can be summarized by the following steps:

Step 1: At iteration $k = 0$ assume random values for the of the membrane parameters within their respective ranges $\boldsymbol{x}_{2:N}^{(k)}$.

Step 2: Compute the outputs of the previously trained network for all the frequencies of interest f_m:

$$y_m^{(k)} = \boldsymbol{f}\left(\left[f_m, \boldsymbol{x}_{2:N}^{(k)}\right]^{\boldsymbol{T}}, \boldsymbol{\theta}^*\right), m = 1 : M.$$

Step 3: Compute the sum-squared error: $\boldsymbol{E}(\boldsymbol{x}^{(k)}) = ||\boldsymbol{r}^d - \boldsymbol{y}^{(k)}||^2$

Step 4: Compute the gradient of $\boldsymbol{E}(\boldsymbol{x}^{(k)})$ with respect to $\boldsymbol{x}_{2:N}^{(k)}$ and update $\boldsymbol{x}_{2:N}$: $\boldsymbol{x}_{2:N}^{(k+1)} = \boldsymbol{x}_{2:N}^{(k)} - \eta\nabla_{\boldsymbol{x}} E(\boldsymbol{x}_{2:N}^{(k)})$,

Step 5: Go to Step 2 and repeat until $\boldsymbol{E}\left(\boldsymbol{x}^{(k)}\right) < Threshold$ or $k = k_{\max}$

Generation of training data. The first step in the process of constructing a forward data driven model consists of generating a representative dataset with known ground-truth that captures different characteristics of the membrane-type acoustic metasurface under investigation. To this end, we generated a realistic dataset D of sound absorption responses for a range of membrane geometric parameter values using numerical simulations. The independent model parameters considered in this study consist of the membrane radius ($a \in [20, 60]$mm), thickness ($h \in [0.01, 0.5]$mm) and cavity depth ($e_c \in [1, 40]$mm). The

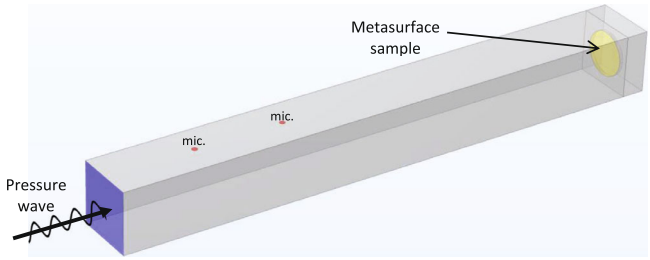

Fig. 3 Schematic of the impedance tube configuration. The normal sound absorption ground truth was simulated for randomly generated membrane parameter combinations, covering a frequency range of 1 to 3000 Hz with 3 Hz increments.

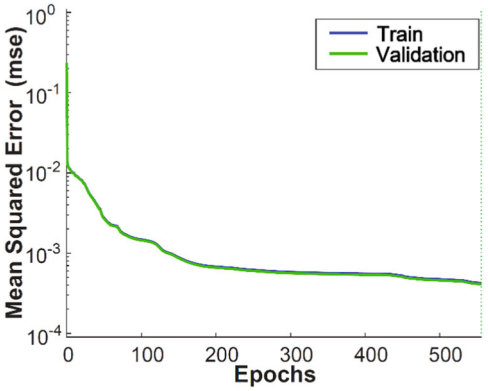

Fig. 4 Mean square error loss of the training and validation sets as a function of training epochs. Both the training and validation errors exhibit similar characteristics, showing a decreasing trend as the number of epochs increases. The model achieves the lowest validation MSE of 0.0004 at epoch 556.

focus on geometrical parameters is justified by the strong dependence of the acoustic response on membrane geometry. The elastic constants of the material were selected from COMSOL material library as a stainless steel and are considered to be fixed including the Young's modulus ($E = 2 \cdot 10^{11}$ Pa), mass density ($\rho = 7850\,\mathrm{kg\,m^{-3}}$]), Poison's ratio ($\nu = 0.27$) and effective loss coefficient ($\xi = 0.0613$). The independent parameters are drawn randomly from uniform distributions within their respective ranges.

The FE software COMSOL was used to calculate the acoustic wave reflections in an environment that mimics measurements in an impedance tube according to the ISO 10534-2 protocol. The cylindrical membrane assumed to be backed by an air cavity and clamped in a tube with a square outer section and circular inner hollow section. The acoustical behavior of the membrane is investigated inside a rectangular impedance tube of inner width equals to the outer width of the clamping cube. A unit pressure is applied on the opposite side of the membrane to serve as a normal incidence excitation. The acoustic pressure interacts with the elastic vibration mode of the membrane inducing sound losses through the visco-thermal effect modeled as an absorbed thin layer attached to the membrane. The simulation configuration is shown in Fig. 3. For each combination of the independent parameters, the normal sound absorption coefficient was recorded for the frequency range 1 to 3000 Hz in 3 Hz increments.

Forward model Network architecture. The aim is to train a feedforward neural network to approximate the physics-based membrane model using the training inputs and corresponding targets. The selection of the network topology in terms of number of layers and neurons at each hidden layer is usually found with several trial-and-error training runs. Larger networks can create more complex functions with the risk of overfitting. i.e., small error on the training set and large error on unseen data. Preventing overfitting can be achieved either through regularization, early stopping or by increasing the size of the training set. In this study, the network size was kept large enough to provide a good fit while the size of the training set was increased to ovoid overfitting. A neural network with 5 hidden layers and out output (4-24-16-8-4-1) was trained using 50 million data points (100 thousand absorption profiles each contains 500 frequencies). The actual network inputs comprise the membrane radius a, thickness h, cavity depth e_c, and frequency (f). The desired output is the normal absorption coefficient (α) at the frequency f. Prior to training, the data is partitioned into three subsets training, validation, and test sets, with ratios 70%, 15%, and 15%, respectively. All hidden layers use the standard logistic sigmoid activation function, while the output neuron uses a linear activation function. The network was trained using the Levenberg-Marquardt algorithm, which is characterized by an efficient update rule that varies between the gradient descent and the Gauss-Newton method.

Figure 4 shows the plots of the mean squared error (MSE) loss as a function of the number of training epochs for the training and validation sets. The training and validation errors exhibit similar characteristic, a decreasing function of the number of epochs. The model achieves the lowest validation MSE of 0.0004 at epoch 556. The agreement between the actual and predicted values is further evaluated statistically through Pearson's correlation coefficient (R) between the model output relative to FEM's desired output. The model performed well with a correlation coefficient of over 0.98.

Figure 5 illustrates the network response as a function of frequency for four different sets of input parameters chosen from the test set, except for Fig. 5d whose one of its parameters was chosen outside the range of the training parameters. The physical parameter sets {radius, thickness, depth} used were: (a) {45.5, 0.37, 27.5} mm, (b) {33.4, 0.02, 26.5} mm, (c) {45, 0.04, 7.5} mm, and (d) {32, 0.025, 54} mm. The curves are produced by fixing the physical parameters (a, h, and e_c) and varying the input frequency. The sound absorption curves generated based on the learned model show high fidelity with those based on the FEM simulation across different spectral patterns. Figure 5a, b show resonator responses with one and two prominent peaks, respectively. Figure 5c is a broadband absorber with a relative bandwidth of 15% for an absorption coefficient $\alpha = 0.8$ at the frequency $f = 1165$ Hz.

The ability of the model to generalize beyond the range of the training parameters is also evaluated by generating the broadband spectrum of Fig. 5d. This spectrum is generated with a cavity depth $e_c = 54$ mm, a relative bandwidth of 31%, and $\alpha = 0.6$ around the central frequency $f_c = 509$ Hz. The plots in Fig. 5 clearly show that the trained model produces sound absorptions that are in good agreement with the simulated FEM responses. The correlation coefficients between the model and the FEM responses in these examples were greater than 0.99. The proposed forward model resulted in a speed improvement of over four orders of magnitude compared to FEM simulation on a typical personal computer.

Inverse design of membrane-type metasurface absorber. The membrane absorbers presented in this study are characterized by high and narrow absorption peaks at specific frequencies. Broader frequency absorption using these structures can be achieved through the coupling of the high-order elastic modes of the single

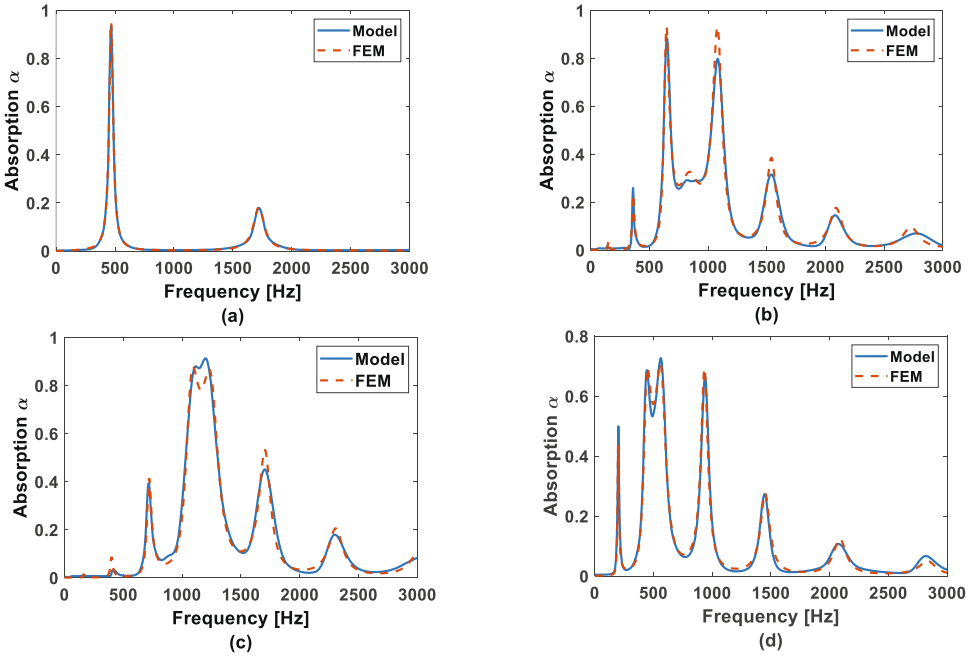

Fig. 5 The model predicted absorption spectrum and the COMSOL simulated FEM responses. The blue curve represents the model predicted absorption spectrum, while the red curve represents the COMSOL simulated FEM response for four different sets of parameters {radius, thickness, depth}: **a** {45.5, 0.37, 27.5} mm, **b** {33.4, 0.02, 26.5} mm, **c** {45, 0.04, 7.5} mm, and **d** {32, 0.025, 54} mm.

membrane. These couplings occur with specific geometrical parameters of the membrane and the air cavity. They are, however, not easy to describe using simple analytical models. This section aims to illustrate the application of the proposed inverse design approach to realize absorbers with prominent absorption peaks at selected subwavelength frequencies and broadband absorbers. In the following, we describe the estimation of the membrane parameters for a given reference absorption profile.

Reference absorption profile and parameters estimation. Depending on the intended response of the absorber, a desired (reference) absorption profile $\boldsymbol{r}^d$ should be first defined. The membrane parameters $\boldsymbol{x}^*$ are then estimated by minimizing the deviation between the model output $\boldsymbol{y}$ and $\boldsymbol{r}^d$ using the inverse design approach. The algorithm remains the same, except that the error computation in Step 3 of the iterative inversion approach should include only the frequency range or the frequency values of interest. The algorithm starts from a random initial point $\boldsymbol{x}^0$ and produces a sequence of parameter estimates $\boldsymbol{x}^k$ $(k = 0, 1, 2, \ldots)$ with the objective to minimize the cost function $E(\boldsymbol{x}) = ||\boldsymbol{r}^d - \boldsymbol{y}(\boldsymbol{x})||^2$. Depending on the starting point $(\boldsymbol{x}^0)$, the algorithm might converge to different local minima; this is due to the fact that different combination of parameters may yield similar values of the cost function. Different random initial values are evaluated, and the best fit is presented. In this section, three case studies are presented: single narrow-band, dual narrow-band, and wideband absorber. Here, we consider only the frequency range covered by the impedance tube (up to 1500 Hz).

a. **Single narrow-band absorber:** One way to define the reference absorption profile $\boldsymbol{r}^d$ is using the frequency response of a second-order resonator of the form:

$$H(s) = K\frac{s}{s^2 + \Delta\omega_p s + \omega_p^2}, \tag{8}$$

b. where K is a constant gain, $\Delta\omega_p$ represents the half-power (3 dB) bandwidth, and $\omega_p = 2\pi f_p$ is the peak or resonant frequency. The bandwidth is inversely proportional to the Q-factor Q_p, $\Delta\omega_p = \omega_p/Q_p$. Figure 6 shows an example of a reference absorption spectrum (green dashed line) with absorption level $\alpha = 1$ at $f_p = 1252$ Hz and Q-factor $Q_p = 32$, along with the forward model response (blue dotted line), using as input the estimated membrane parameters, and FEM responses (red solid line). The estimated membrane parameters are summarized in Table 1. The model response is highly correlated with the desired response around the peak frequency. It contains a second small peak at frequency $f = 624$ Hz. The model response is validated numerically using FEM simulation, and the two responses match very well.

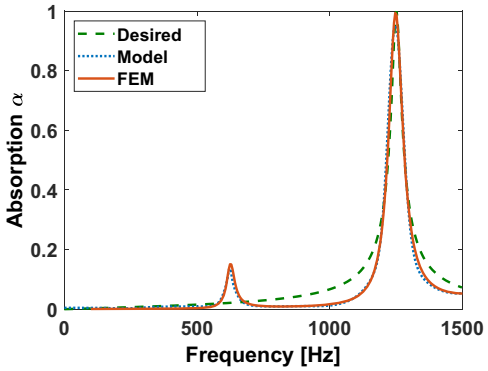

Fig. 6 Desired, estimated, and FEM simulated single narrow-band absorber responses. The reference absorption profile (dashed line) is defined by the amplitude frequency response of a second-order resonator. The forward model response (dotted line), using as input the estimated membrane parameters, closely aligns with the desired response around the peak frequency of $f_p = 1{,}252$ Hz, exhibiting an absorption level $\alpha = 1$ and a Q-factor $Q_p = 32$. The actual absorption response of the absorber achieved through FEM simulation is shown as a solid line.

Table 1 Estimated membrane parameters.

Estimated parameters	Simple absorber	Dual-band absorber	Wideband absorber
Radius a (mm)	25.5	24.7	30.9
Thickness h (mm)	0.0509	0.0500	0.0247
Cavity depth e_c (mm)	4.0	13.5	16.9

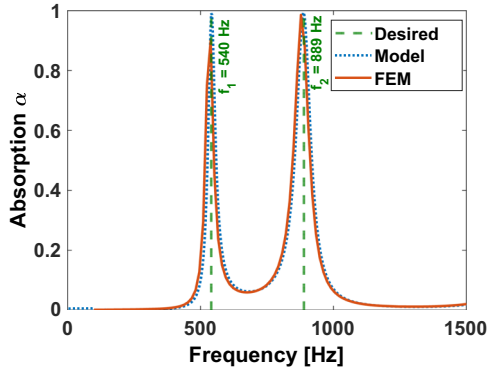

Fig. 7 Dual narrow-band absorber characteristics. The desired membrane absorption characteristic (dashed line) with absorption coefficient $\alpha = 1$ at frequencies $f_1 = 540$ Hz and $f_2 = 889$ Hz. The forward model response (dotted line) has a maximum absorption coefficient $\alpha = 0.99$ at the desired frequencies. The FEM simulated response (solid line) has a slightly lower absorption coefficient, $\alpha = 0.9$, at f_1.

c. **Dual narrow-band absorber:** The reference response in this case can be defined as the desired absorption coefficient (α) at specific frequencies f_1 and f_2. Figure 7 is an example of a reference response (green dashed line) with $\alpha = 1$ at $f_1 = 540$ Hz and $f_2 = 889$ Hz. The model response (blue dotted line) using as input the estimated membrane parameters and the FEM simulation (red solid line) are also included. The estimated membrane parameters are summarized in Table 1. The inverse parameters estimation yielded an absorption coefficient values equal to 0.99 at the selected frequencies. The model response is very close to the response obtained with FEM simulation. It is worth mentioning that the FEM response shows a slightly lower absorption coefficient ($\alpha = 0.9$) at f_1.

Wideband absorber: The reference response in this case can be the desired absorption coefficient (α) over the specific frequency band of interest. Figure 8 is an illustration of an ideal bandpass response (green dashed line) with a relative bandwidth of 23% for $\alpha = 0.8$ around the central frequency $f_c = 97$ Hz. The forward model (blue dotted line) and the desired response display similar behavior in terms of general tendencies. The discrepancies between the two spectra are due to the limitations imposed by the inherent behavior of the membrane's resonance as well as the fact that the desired response is an ideal response that cannot be achieved by real causal system and can only be approximated. The forward model response, using as input the estimated membrane parameters, correlates well with the simulated FEM response (red solid line).

Experimental results. Based on findings summarized in Table 1, we selected the single and the dual narrow band absorbers for fabrication. The experimental results show a good agreement with the estimated absorption spectrum (α_{FEM1}) in terms of general tendencies and spread around the peaking frequency. The main

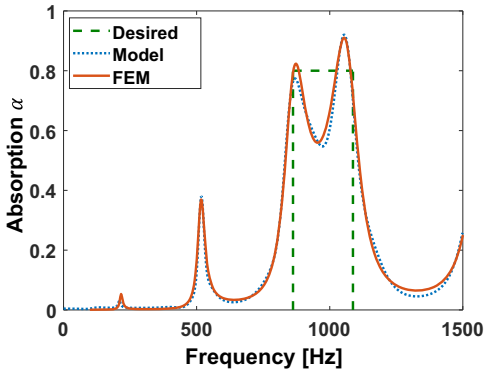

Fig. 8 Wideband absorber characteristics. The desired wideband characteristic (dashed line) is an ideal bandpass response with a relative bandwidth of 23% for $\alpha = 0.8$ around the center frequency $f_c = 97$ Hz. The forward model response (dotted line), using as input the estimated membrane parameters, correlates well with the simulated FEM response (solid line).

difference between the results in the case of single narrow-band (Fig. 9a) is a shift in the frequency response of the experimental absorption curve towards the higher frequencies with a relative frequency shift of about 3% and a 1.8% decrease of the value of the resonance amplitude. Similar behavior was observed with the dual narrow-band absorber (Fig. 9b) with a slight difference in the shift between the first and second prominent peaks.

Replacing the COMSOL default value of the Young Modulus (E = 20 GPa) used in the first simulation (blue curve in Fig. 9) by the actual value (E = 27 GPa) of the reinforced stainless steel used in the experiment resulted in an upward shift in resonance frequencies (red curve in Fig. 9) towards the experimental values. Other shifts and discrepancies are due to modeling errors caused by the deformation in the fabrication of the 3D-printed frame and the inaccuracies that occur during the assembly process. In the numerical model, we assumed rigid condition on the lateral boundaries of the membrane, which is very difficult to achieve experimentally. Practically, sandwiching and pressing the steel membrane between the rigid frame induces a static stress in the clamped boundary, which affects the mechanical vibration and results in a shift of the resonant frequency.

Conclusion

This study presented a systematic framework for the forward modeling and inverse design of membrane-type metasurfaces sound-absorbers. Once trained, the forward model reduces the computational time by orders of magnitude compared to conventional approaches. The iterative inversion method finds the input that reconstructs the desired output when cascaded with the forward model. We validated the proposed approach numerically and experimentally. This data-driven approach simplifies the way of designing metasurfaces with desired acoustic properties.

Methods

Fabrication of the membranes. The elasto-acoustic metasurfaces selected for fabrication consist of a circular membrane backed by an air cavity with rigid endings. Each device is made up of two polymer cuboids with cylindrical cavities and a steel sheet membrane. The cuboids were created layer-by-layer using an additive manufacturing technique. For the first device, the first cuboid is of dimension $70 \times 70 \times 10$ mm with a cylindrical cavity of radius $a = 25.5$ mm and a cavity depth $e_c = 4$ mm. The second cuboid has a dimension of $70 \times 70 \times 5$ mm with a cylindrical hollow air cavity of radius $a = 25.5$ mm. For the second device, the first cuboid is of dimension $70 \times 70 \times 10$ mm with a cylindrical cavity of radius $a = 24.7$ mm and a cavity depth $e_c = 13.5$ mm. For both devices, a membrane of a side length of 70 mm and a thickness of 0.05 mm was sandwiched between the cuboids and secured using eight cap screws. Figure 10a, b, which display the schematic and fabricated membrane, respectively.

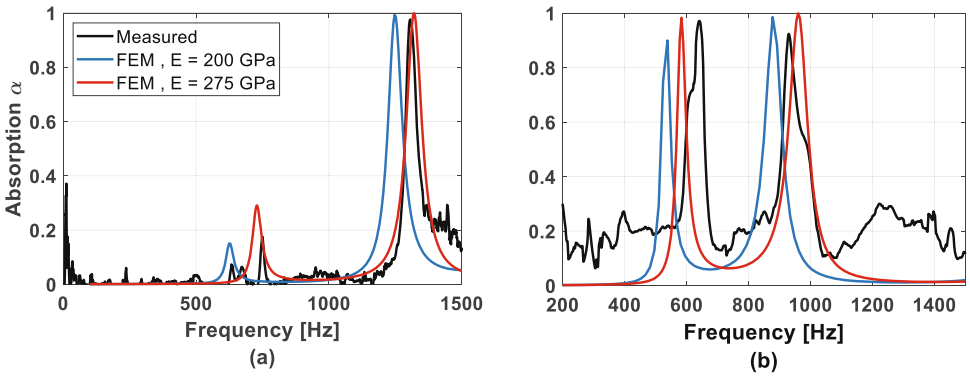

Fig. 9 Measured and FEM simulated absorption spectra with COMSOL default and actual Young modulus for single and dual narrow-band absorbers. **a** Single narrow -band absorber. **b** Dual narrow-band absorber. The black curve represents the measured spectrum, the blue curve represents the absorption spectrum obtained using the COMSOL default Young modulus, while the red curve represents the absorption spectrum with the actual Young modulus.

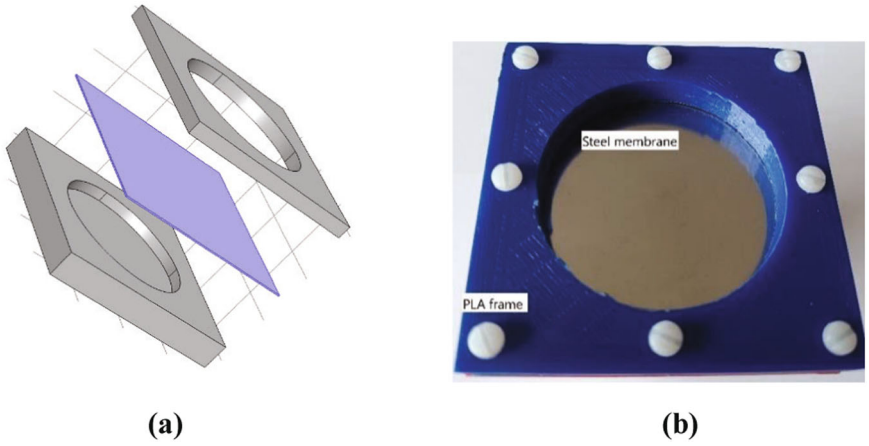

Fig. 10 Example of a fabricated sound absorption device. a Schematic representation of the device design. **b** Photograph of the fabricated device highlighting its key components.

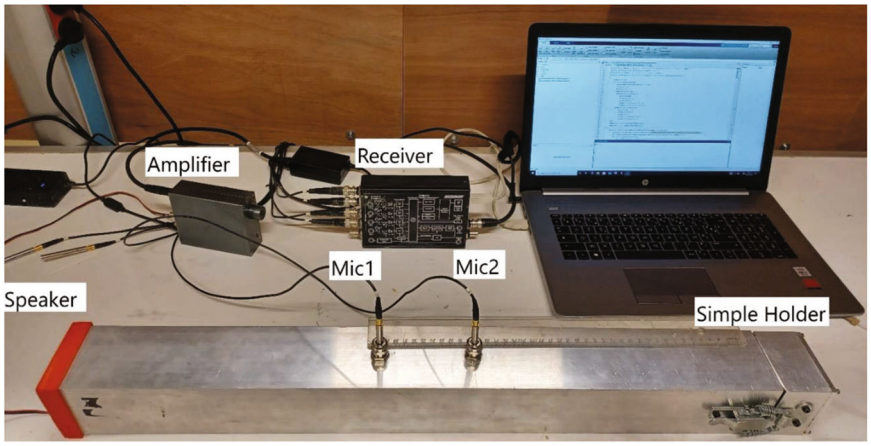

Fig. 11 Experimental setup for the impedance tube measurements. The experiment utilized a non-commercial impedance tube apparatus based on the two-microphone transfer function method, following the ISO 10534-2 protocol.

Experimental protocol. A non-commercial impedance tube apparatus based on the Two-Microphone transfer function method specified in the ISO 10534-2 protocol was used in this experiment, see Fig. 11. It serves at determining the complex reflection factor (R) and the dimensionless sound absorption coefficient (α) curve of the metasurface at different frequencies for normal sound incidence. The apparatus consists of a rigid rectangular impedance tube of inner cross section of 7×7 cm and length 60 cm, a loudspeaker mounted on one end of the tube, the metasurface membrane mounted at the other end and two identical microphones located on the side of the membrane to measure the acoustic pressure of the incident and reflected waves inside the tube. The two microphones are respectively located at 20 cm and 30 cm away from the surface of the structure. The loudspeaker generates broadband random signal covering the frequency range of interest namely, 50 to 1500 Hz. The pressure signals measured at the microphones are used to solve the pressure equation in the tube:

$$p(x) = p_0\left(e^{jkx} + Re^{-jkx}\right), \tag{9}$$

where p_0 is a constant; k is the wavenumber; the membrane is assumed to be at $x = 0$. The first and the second term in (9) represent respectively the incident and reflected waves.

By computing transfer function, ratio of pressures $H_{12} = \frac{p(x_2)}{p(x_1)}$, at the two microphone positions we can solve for the refection factor $\left(R = \frac{H_{12}e^{jkx_1} - e^{jkx_2}}{e^{-jkx_2} - H_{12}e^{jkx_1}}\right)$ and deduce the absorption coefficient as $\alpha = 1 - |R|^2$.

The generated signals were amplified then processed using a multi-channel high-accuracy dynamic signal acquisition module connected to a computer for data analysis.

Data availability

The data that support the findings of this study are available from the corresponding author upon reasonable request.

Code availability

The code used for this study are available from the corresponding author upon reasonable request.

Received: 1 May 2022; Accepted: 17 May 2023;
Published online: 29 May 2023

References

1. Smith, D., Padilla, W., Vier, D., Nemat-Nasser, S. & Schultz, S. Composite medium with simultaneously negative permeability and permittivity. *Phys. Rev. Lett.* **84**, 4184–4187 (2000).
2. Bessa, M. A., Glowacki, P. & Houlder, M. Bayesian machine learning in metamaterial design: Fragile becomes supercompressible. *Adv. Mater.* **31**, 1904845 (2019).
3. Khatib O., Ren S., Malof J., Padilla W. J. Deep learning the electromagnetic properties of metamaterials—a comprehensive review. *Adv. Funct. Mater.* 28:2101748 (2021).
4. Assouar, B. et al. Acoustic metasurfaces. *Nat. Rev. Mater.* **3**, 460–472 (2018).
5. Zhu, J., Zhu, X., Yin, X., Wang, Y. & Zhang, X. Unidirectional extraordinary sound transmission with mode-selective resonant materials. *Phys. Rev. Appl.* **13**, 041001 (2020).
6. Park, J. J., Park, C. M., Lee, K. J. & Lee, S. H. Acoustic superlens using membrane-based metamaterials. *Appl. Phys. Lett.* **106**, 051901 (2015).
7. Liu, Z. et al. Locally resonant sonic materials. *Science* **289**, 1734–1736 (2000).
8. Zhu, J., Zhu, X., Yin, X., Wang, Y. & Zhang, X. Unidirectional extraordinary sound transmission with mode-selective resonant materials. *Phys. Rev. Appl.* **13**, 041001 (2020).
9. Park, J. J., Lee, K. J. B., Wright, O. B., Jung, M. K. & Lee, S. H. Giant acoustic concentration by extraordinary transmission in zero-mass metamaterials. *Phys. Rev. Lett.* **110**, 244302 (2013).
10. Liu, Z. et al. Locally resonant sonic materials. *Science* **289**, 1734–1736 (2000).
11. Elayoucha, A., Addouche, M. & Khelif, A. Extensive tailorability of sound absorption using acoustic metamaterials. *J. Appl. Phys.* **124**, 155103 (2018).
12. Capolino, F., Khajavikhan, M. & Alù, A. Metastructures: from physics to application. *Appl. Phys. Lett.* **120**, 060401 (2022).
13. Qu, S. & Sheng, P. Minimizing indoor sound energy with tunable metamaterial surfaces. *Phys. Rev. Appl.* **14**, 034060 (2020).
14. Li, J., Wen, X. & Sheng, P. Acoustic metamaterials. *J. Appl. Phys.* **129**, 171103 (2021).
15. Yang, M., Chen, S., Fu, C. & Sheng, P. Optimal sound-absorbing structures. *Mater. Horizons* **4**, 673–680 (2017).
16. Li Y. & Assouar B. M. Acoustic metasurface-based perfect absorber with deep subwavelength thickness. *Appl. Phys. Lett.* **108**, 063502.
17. Esfahlani, H., Mazor, Y. & Alù, A. Homogenization and design of acoustic Willis metasurfaces. *Phys. Rev. B* **103**, 054306 (2021).
18. Lan, J. et al. Manipulation of acoustic wavefront by gradient metasurface based on Helmholtz Resonators. *Sci. Rep.* **7**, 10587 (2017).
19. Song, B. H. & Bolton, J. S. A transfer-matrix approach for estimating the characteristic impedance and wave numbers of limp and rigid porous materials. *J. Acoust. Soc. Am.* **107**, 11311152 (1999).
20. Jiménez, N. et al. Broadband quasi perfect absorption using chirped multi-layer porous materials. *AIP Adv.* **6**, 121605 (2016).
21. Li, D., Chang, D. & Liu, B. Enhanced lowto mid.frequency sound absorption using parallelarranged perforated plates with extended tubes and porous material. *Appl. Acoust.* **127**, 316323 (2017).
22. Li, J. & Hesthaven, J. S. Analysis and application of the nodal discontinuous Galerkin method for wave propagation in metamaterials. *J. Comput. Phys.* **258**, 915–30. (2014).
23. Donda, K. et al. Ultrathin acoustic absorbing metasurface based on deep learning approach. *Smart Mater. Struct.* **30**, 085003 (2021).
24. Liu, L. et al. Broadband acoustic absorbing metamaterial via deep learning approach. *Appl. Phys. Lett.* **120**, 251701 (2022).
25. Alguacil, A., Bauerheim, M., Jacob, M. C. & Moreau, S. Predicting the propagation of acoustic waves using deep convolutional neural networks. *J. Sound Vib.* **512**, 116285 (2021).
26. Zhang, H. et al. SAP-Net: deep learning to predict sound absorption performance of metaporous materials. *Mater. Des.* **212**, 110156 (2021).
27. Kumar, S., Tan, S., Zheng, L. & Kochmann, D. M. Inverse-designed spinodoid metamaterials. *npj Comput. Mater.* **6**, 1–0 (2020).
28. Donda, K. et al. Ultrathin acoustic absorbing metasurface based on deep learning approach. *Smart Mater. Struct.* **30**, 085003 (2021). ff10.1088/1361-665X/ac0675f.
29. Bessa, M. A., Glowacki, P. & Houlder, M. Bayesian machine learning in metamaterial design: fragile becomes supercompressible. *Adv. Mater.* **31**, 1904845 (2019).
30. Khatib, O., Ren, S., Malof, J. & Padilla, W. J. Deep learning the electromagnetic properties of metamaterials—a comprehensive review. *Adv. Funct. Mater.* **31**, 2101748 (2021).
31. Lu, B. L., Kita, H. & Nishikawa, Y. Inverting feedforward neural networks using linear and nonlinear programming. *IEEE Trans. Neural Netw.* **10**, 1271–1290 (1999).
32. Kindermann, J. & Linden, A. Inversion of neural networks by gradient descent. *Parallel Comput.* **14**, 277–86. (1990).
33. Jordan, M. I. & Rumelhart, D. E. Forward models: supervised learning with a distal teacher. *Cogn. Sci.* **16**, 307–54. (1992).
34. Peurifoy, J. et al. Nanophotonic particle simulation and inverse design using artificial neural networks. *Sci. Adv.* **4**, eaar4206 (2018).
35. Liu, D., Tan, Y., Khoram, E. & Yu, Z. Training deep neural networks for the inverse design of nanophotonic structures. *ACS Photon.* **5**, 1365–1369 (2018).
36. Ma, W. et al. Deep learning for the design of photonic structures. *Nat. Photon.* **15**, 77–90 (2021).
37. He, L. et al. Machine-learning-driven on-demand design of phononic beams. *Sci. China Phys. Mech. Astronom.* **65**, 214612 (2022).
38. Ding, H. et al. Deep learning enables accurate sound redistribution via nonlocal metasurfaces. *Phys. Rev. Appl.* **16**, 064035 (2021).
39. Wong E. & Kolter J. Z. Neural network inversion beyond gradient descent. OPTML 2017: 10th NIPS Workshop on Optimization for Machine Learning (NIPS 2017)
40. Jensen, C. A. et al. Inversion of feedforward neural networks: algorithms and applications. *Proc. IEEE.* **87**, 1536–49. (1999).
41. Raymond, S. J. et al. A deep learning approach for designed diffraction-based acoustic patterning in microchannels. *Sci. Rep.* **10**, 8745 (2020).

Acknowledgements

A.B. and H.B. work was supported by Qatar Foundation. A.K. and M.A. work was supported by the EIPHI Graduate School under Contract No. ANR-17-EURE-0002.

Author contributions

A.B. and A.K. conceived and directed the project. H.B. and A.B. formulated and implemented the forward and the inverse models. H.B. and A.K. designed the case study scenarios. M.A. conducted the FEM simulation to generate the training set. A.K. and M.A. fabricated the devices and performed the measurements. H.B. wrote the first draft of the manuscript. All authors contributed to data analysis and the revision of the manuscript.

Funding

Open Access funding provided by the Qatar National Library.

Competing interests

The authors declare no competing interests.

Additional information

Correspondence and requests for materials should be addressed to Hamza Baali, Mahmoud Addouche, Abdesselam Bouzerdoum or Abdelkrim Khelif.

Peer review information *Communications Materials* thanks Yong Li and the other, anonymous, reviewer(s) for their contribution to the peer review of this work. Primary Handling Editor: Aldo Isidori.